

# Full bandwidth electrophysiology of seizures and epileptiform activity enabled by flexible graphene micro-transistor depth neural probes

Andrea Bonaccini Calia<sup>1</sup>, Eduard Masvidal-Codina<sup>2</sup>, Trevor M. Smith<sup>4</sup>, Nathan Schäfer<sup>1</sup>, Daman Rathore<sup>4</sup>, Elisa Rodríguez-Lucas<sup>1</sup>, Xavi Illa<sup>2,3</sup>, Jose M. De la Cruz<sup>1</sup>, Elena Del Corro<sup>1</sup>, Elisabet Prats-Alfonso<sup>2,3</sup>, Damià Viana<sup>1</sup>, Jessica Bousquet<sup>1</sup>, Clement Hébert<sup>1</sup>, Javier Martínez-Aguilar<sup>2,3</sup>, Justin R. Sperling<sup>1</sup>, Matthew Drummond<sup>5</sup>, Arnab Halder<sup>5</sup>, Abbie Dodd<sup>5</sup>, Katharine Barr<sup>5</sup>, Sinead Savage<sup>5</sup>, Jordina Fornell<sup>6</sup>, Jordi Sort<sup>6,8</sup>, Christoph Guger<sup>7</sup>, Rosa Villa<sup>2,3</sup>, Kostas Kostarelos<sup>5</sup>, Rob Wykes<sup>4, 5\*</sup>, Anton Guimerà-Brunet<sup>2,3\*</sup>, and Jose A. Garrido<sup>1,8\*</sup>

1 Catalan Institute of Nanoscience and Nanotechnology (ICN2), CSIC and The Barcelona Institute of Science and Technology (BIST), Campus UAB, Bellaterra, Barcelona, Spain.

2 Institut de Microelectrònica de Barcelona, IMB-CNM (CSIC), Esfera UAB, Bellaterra, Spain.

3 Centro de Investigación Biomédica en Red en Bioingeniería, Biomateriales y Nanomedicina (CIBER-BBN), Madrid, Spain.

4 Department of Clinical and Experimental Epilepsy, Queen Square Institute of Neurology, University College London, London, United Kingdom.

5 Nanomedicine Lab, Faculty of Biology Medicine & Health National Graphene Institute, University of Manchester, United Kingdom

6 Departament de Física, Campus UAB, Universitat Autònoma de Barcelona, E-08193 Bellaterra, Barcelona, Spain

7 g.tec medical engineering GmbH, Guger Technologies OG, Austria

8 ICREA, Barcelona, Spain

\* Corresponding authors: [joseantonio.garrido@icn2.cat](mailto:joseantonio.garrido@icn2.cat); [r.wykes@ucl.ac.uk](mailto:r.wykes@ucl.ac.uk); [anton.guimera@imb-cnm.csic.es](mailto:anton.guimera@imb-cnm.csic.es)

## **ABSTRACT:**

**Mapping the entire frequency bandwidth of neuronal oscillations in the brain is of paramount importance for understanding physiological and pathological states. The ability to record simultaneously infraslow activity (<0.1 Hz) and higher frequencies (0.1-600 Hz) using the same recording electrode would particularly benefit epilepsy research. However, commonly used metal microelectrode technology is not well suited for recording infraslow activity. Here we use flexible graphene depth neural probes (gDNP), consisting of a linear array of graphene microtransistors, to concurrently record infraslow and high frequency neuronal activity in awake rodents. We show that gDNPs can reliably record and map with high spatial resolution seizures, post-ictal spreading depolarisation, and high frequency epileptic activity through cortical laminae to the CA1 layer of the hippocampus in a mouse model of chemically-induced seizures. We demonstrate functionality of chronically implanted devices over 10 weeks by recording with high fidelity spontaneous spike-wave discharges and associated infraslow activity in a rat model of absence epilepsy. Altogether, our work highlights the suitability of this technology for *in vivo* electrophysiology research, in particular, to examine the contributions of infraslow activity to seizure initiation and termination.**

## **MAIN TEXT:**

In recent years there has been a resurgence of interest in fluctuations in brain activity occurring at <0.1 Hz, commonly referred to as infraslow activity (ISA)<sup>1</sup>. Several pathological brain states including stroke, traumatic brain injury and migraine with aura are associated with ISA, which can manifest as a slow wave of depolarisation through brain tissue<sup>2</sup>. Interestingly, in the case of epilepsy both fast activity, at hundreds of Hertz (Hz) or higher, and infraslow activity (ISA), at less than 0.5 Hz can be associated with seizures and epileptiform activity<sup>3</sup>. Moreover, seizure generation has been hypothesised to be generated by a coupled dynamical system in which there are fast and slow processes<sup>4</sup>. However, the relationship between these two types of brain activity is poorly understood. A limitation in studying ISA, either independently or concurrently with higher frequency activity is the lack of appropriate tools to record it electrographically *in vivo* with high spatiotemporal fidelity. Experimentally ISA is usually recorded using solution-filled glass micropipettes with Ag/AgCl wires which limits the spatial resolution to just a few-point measurements. A further issue with glass pipettes is that they are not practical for long-term chronic recordings in awake animals and are incompatible with clinical use. To enhance the spatial resolution and long-term recordings, microelectrode grids can be used, however this is not optimal since they suffer from polarization-induced drift and signal attenuation causing distortion of the measured signal<sup>5</sup>. Consequently, research investigating the relationship between ISA and higher frequency activity, either in normal or pathological brain, is hampered by a lack of appropriate technology.

An alternative to commonly used passive electrodes are field-effect transistors (FETs), which are active transducers offering significant advantages in electrophysiology, in particular the capability to monitor infraslow signals<sup>6</sup>. Among the few FET technologies that have been validated for *in vivo* electrophysiology, graphene-based technology is particularly attractive because of the combination of special properties of this material, including chemical and electrochemical inertness, high electrical mobility, biocompatibility, as well as a facile integration into flexible and ultrathin substrates<sup>7</sup>. Recent reports demonstrate the potential of graphene solution-gated field-effect transistors (gSGFETs) for neural interfacing<sup>8,9</sup>. A first proof-of-concept demonstration using epicortical gSGFET arrays for mapping chemically-induced ISA in anesthetized rats has been reported<sup>6</sup>. To advance this technology further, we have developed implantable flexible graphene depth neural probes (gDNP) capable of recording localised full bandwidth

56 neuronal activity, through cortical columns and sub-cortical structures in preclinical rodent models of induced seizures and chronic  
57 epilepsy.  
58 Here, we demonstrate a wafer-scale microtechnology process to fabricate gDNPs consisting of a linear array of graphene micro-  
59 transistors imbedded in a polymeric flexible substrate. In order to penetrate through the mouse cortex and reach the hippocampus  
60 without buckling, we adapted an insertion protocol that uses silk-fibroin (SF)<sup>10,11</sup> to temporarily stiffen flexible gDNPs. We validate  
61 experimentally the ability to detect electrophysiological biomarkers of epileptiform activity, including high frequency oscillations  
62 (HFOs)<sup>12,13</sup> comparable to conventional microelectrodes and we highlight the suitability of graphene transistor technology to record  
63 concurrently additional biomarkers in the infraslow frequency range<sup>14</sup>. These include DC shifts preceding seizure onset<sup>15,16</sup> and post-  
64 seizure spreading depressions<sup>17</sup>, accentuating the potential of this technology to gain mechanistic insight into the involvement of  
65 infraslow activity associated with seizures *in vivo* in awake brain.

## 67 Results

68 **Microfabrication and characterization of the gDNPs.** A graphene-based SGFET is a three terminal device in which single layer  
69 CVD graphene is used as the channel material in contact with the drain and the source terminals. Graphene is the sensing part of the  
70 device directly exposed to the neural tissue. The current in the graphene channel can be modulated or pinned by a third terminal given  
71 by a reference electrode (gate) which is also in contact with the conducting neural tissue (Fig. 1a). Thus, variations in the electrical  
72 potential in the tissue can be transduced into variations of the channel current; this transduction mechanism has been shown to offer  
73 a very versatile sensing platform for electrophysiology<sup>18,19</sup>. The flexible gDNP is a linear array of 14 recording transistors, each with  
74 an active area of 60x60  $\mu\text{m}$ , and a pitch of 100  $\mu\text{m}$ . The probe's tip design consists of a polyimide shank of 200  $\mu\text{m}$  width and 1.6 mm  
75 length (Fig. 1b). gDNPs are fabricated on a 10  $\mu\text{m}$  thick flexible polyimide (PI) substrate using a wafer-scale microfabrication process  
76 previously reported<sup>9</sup> (see Methods). A two-level metallization strategy, with metal levels interconnected using via-holes (Fig. 1b),  
77 reduces track resistance and improves sensor performance. To characterize gDNPs in saline solution we measure simultaneously the  
78 drain-source current ( $I_{\text{DS}}$ ) versus the applied gate-source voltage ( $V_{\text{GS}}$ ) for all the transistors on the shank with a fixed drain-source  
79 voltage ( $V_{\text{DS}}$ ) using customized electronics (see Methods). The transistor sensitivity is a function of its transconductance ( $g_{\text{m}}$ ), defined  
80 as  $g_{\text{m}} = dI_{\text{DS}}/dV_{\text{GS}}$ , which is directly linked to the ability of the gSGFET to amplify recorded signals. gSGFETs exhibit very high  $g_{\text{m}}$   
81 values due to the large capacitive coupling at the graphene-electrolyte interface and to the very high charge carrier mobility of  
82 graphene<sup>20</sup>. Fig. 1c shows the transfer curves as well as the normalized transconductance ( $g_{\text{m}}/V_{\text{DS}}$ ), for all 14 gSGFETs of an exemplary  
83 gDNP device. The small dispersion of the charge neutrality point (CNP), defined as the value of  $V_{\text{GS}}$  where the  $I_{\text{DS}}$  reach its minimum,  
84 attests for the homogeneity of the gDNP. This is crucial for its operation *in vivo* because all transistors share a common source terminal.  
85 Furthermore,  $g_{\text{m}}$  shows a very stable response in a wide applied gate frequency range (up to 5 kHz), both in the hole regime,  $V_{\text{GS}} <$   
86  $V_{\text{CNP}}$ , and in the electron regime,  $V_{\text{GS}} > V_{\text{CNP}}$  (Fig. 1d). Such constant frequency response is important for a proper calibration of the  
87 recorded signals<sup>21</sup>. The detection limit of the sensors is evaluated by means of the effective gate noise ( $V_{\text{RMS}}$ ) integrated between 1  
88 Hz and 2 kHz, with averaged values between 25-30  $\mu\text{V}$  for all fabricated gDNPs (see Supplementary Fig. S2).

89  
90 **Stiffening of the flexible gDNP using silk-fibroin.** gDNPs are highly flexible, compared to traditional rigid depth electrodes, and  
91 although flexibility is highly advantageous once inserted into the tissue, this provides a challenge during insertion. To insert these  
92 probes we temporarily stiffen the gDNP using silk-fibroin (SF)<sup>10,11</sup>. Compared to other natural biopolymers, SF offers excellent  
93 mechanical properties, extremely good biocompatibility, biodegradability, and the versatility of structural readjustments<sup>22,23,24</sup>.  
94 Further, the byproducts of the SF degradation by enzymes (e.g. proteases) have low antigenicity and non-inflammatory  
95 characteristics<sup>25,26</sup>. The stiffening technique (see Methods and Fig. S3) consists of a moulding process in which the gDNP is back-  
96 coated with cured SF, allowing the preparation of a rigid, straight shank with a defined shape and thickness. We tuned the thickness  
97 of the SF by controlling the mould's trench depth, achieving two typical thicknesses of  $80 \pm 10 \mu\text{m}$  and  $150 \pm 12 \mu\text{m}$ , as shown in the  
98 scanning electron microscopy image of Fig. 1e. Mechanical assessment of the SF coated gDNP was performed using a buckling test,  
99 in which the perpendicularly positioned probes were driven against a flat and hard surface (Fig. 1f). An initial linear increase in force  
100 is observed for both coating thicknesses tested, while the probes remained straight before buckling (green box in Fig. 1f). Continued  
101 application of force results in buckling and bending (orange box in Fig. 1f), characterized by a peak in the force-displacement curve.  
102 The obtained peak forces,  $101 \pm 21 \text{ mN}$  for the 150  $\mu\text{m}$  thick SF and  $29 \pm 13 \text{ mN}$  for 80  $\mu\text{m}$  thick SF, are in good agreement with the  
103 previously reported values of peak forces of similar SF-coated neural probes<sup>11,27</sup>. In order to evaluate the effect of the stiffening and  
104 insertion procedures on the device performance, we electrically characterized the gDNPs before and after the SF stiffening process,  
105 as well as before and after insertion and removal from an agarose gel brain model. Fig. 1g shows the averaged values of the normalized  
106  $g_{\text{m}}$  as well as the effective gate noise ( $V_{\text{RMS}}$ ) of all 14 transistors on a gDNP, confirming that neither the stiffening process nor the  
107 insertion in an agarose brain model impair gDNP performance in terms of transconductance nor noise. Video frames of a SF-coated  
108 gDNP inserted in an agarose brain model (Fig. 1h) show the fast water absorption (<10 s) of SF after complete insertion (insertion  
109 speed: 400  $\mu\text{m/s}$ ) as well as the collapsing of the SF in small residue beads which often stays in the solution for a longer period of  
110 time. As observed from the gDNP after removal from agar gel (180 s), SF is completely delaminated from the polymeric shank,  
111 therefore making the SF coated probes suitable for single-time insertion.

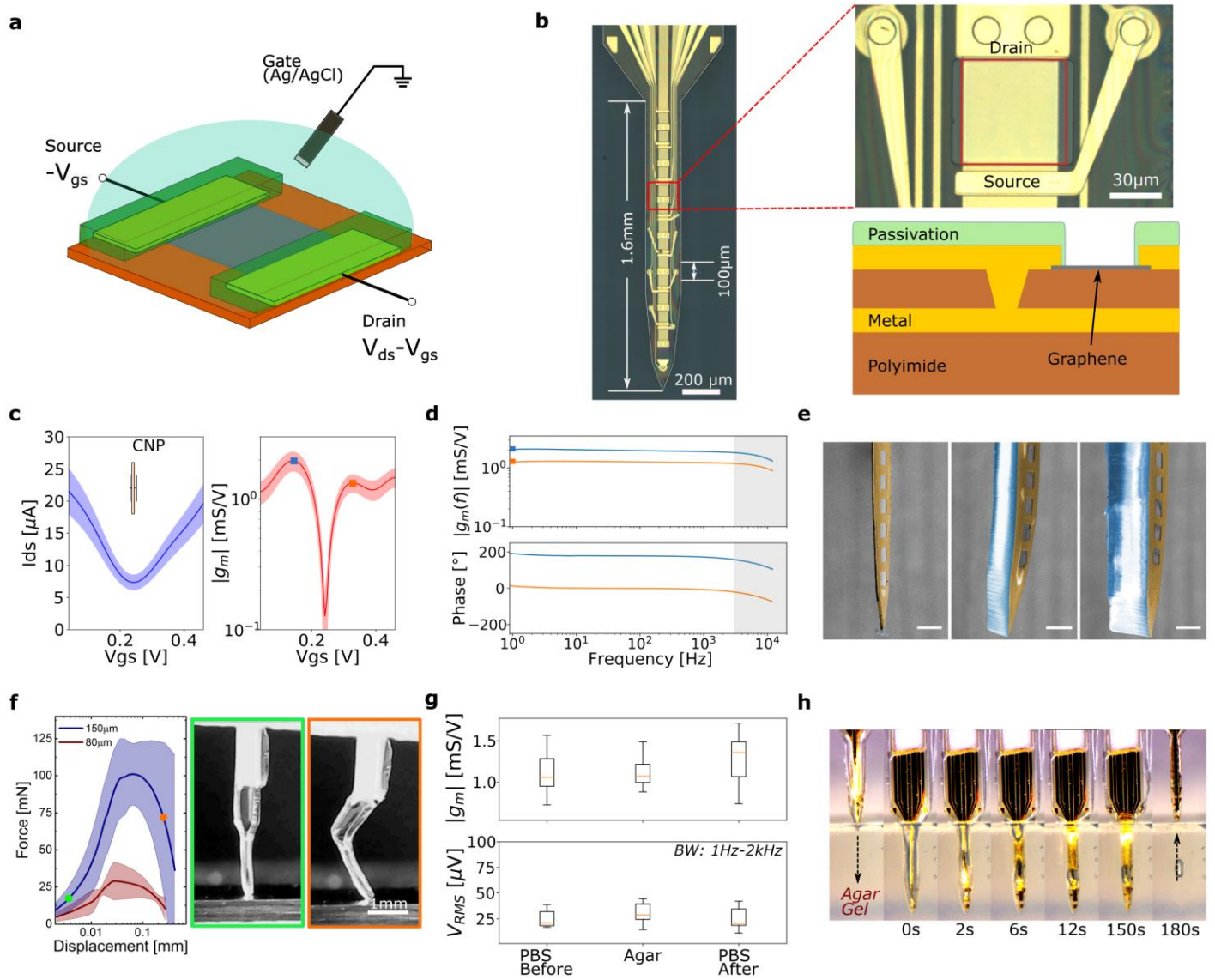
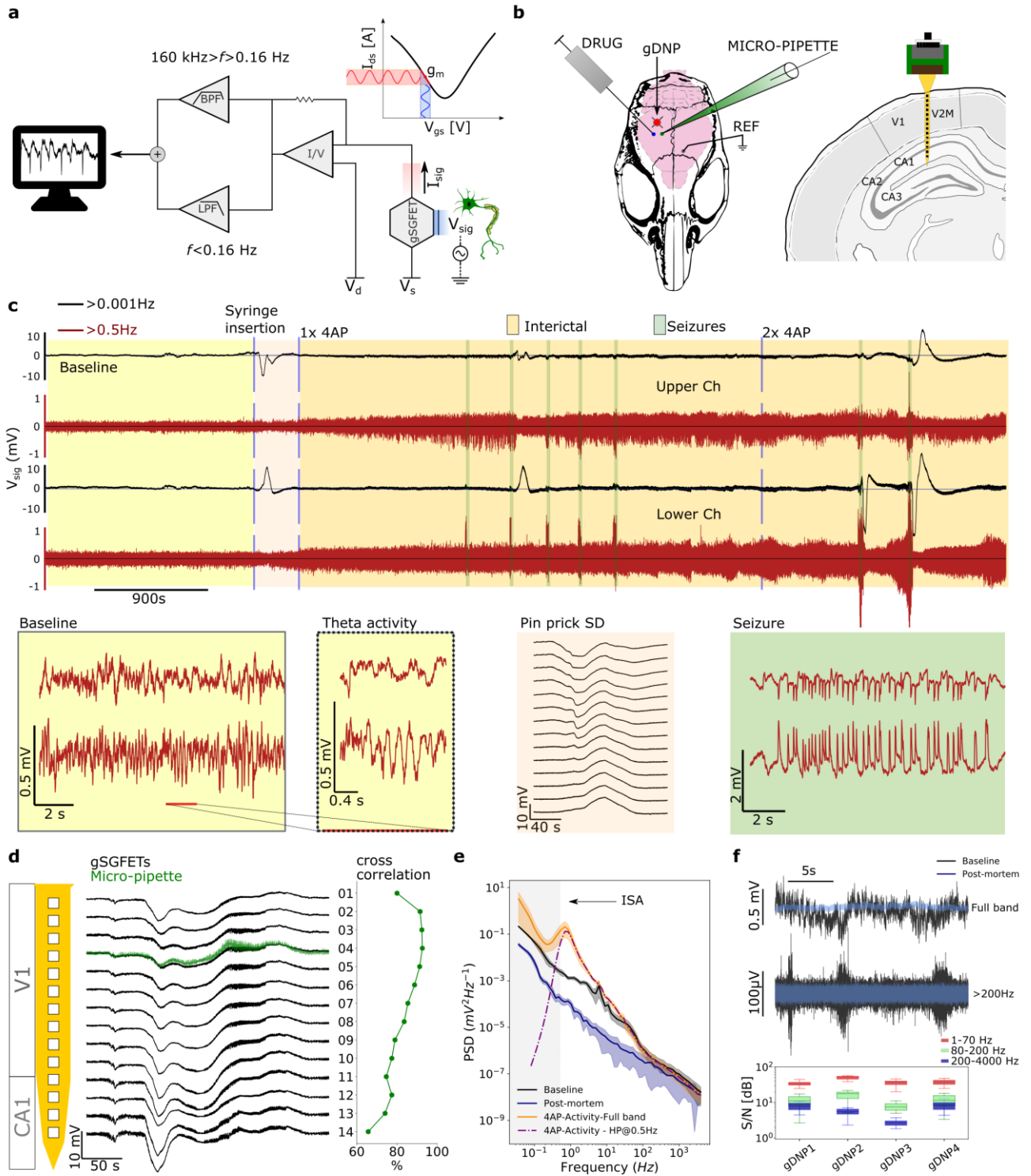


**Fig. 1 Flexible graphene Depth Neural Probe (gDNP) technology and characterization.** **a**, Schematic of a graphene solution-gated field-effect transistor (gSGFET) and biasing.  $V_{gs}$ : gate-source voltage,  $V_{ds}$ : drain-source voltage. **b** Optical microscope image of a gDNP containing 14 transistors with a pitch of 100  $\mu\text{m}$  on a 200  $\mu\text{m}$  wide polyimide shank. Right: blown up image of one gSGFET; the red contour highlights the graphene sensing area (60x60 $\mu\text{m}$ ) of the transistor. The schematic of the cross section of one transistor shows the interconnected metal tracks strategy to reduce the shank width of the gDNP. **c-d**, Electrical characterisations of all 14 gSGFET on a gDNP in a 150 mM saline solution ( $V_{ds} = 50$  mV). **c**, Mean values with standard deviation (shaded colours) of drain-source current ( $I_{ds}$ ) and transconductance ( $g_m$ ) versus  $V_{gs}$ . **d**, Transconductance spectroscopy of the gSGFET bias at the point of maximum  $g_m$  in the electron ( $V_{gs} > V_{CNP}$ , orange line) and hole regime ( $V_{gs} < V_{CNP}$ , blue line). Squares dots are the values of the  $g_m$  as measured in steady-state mode. The decay observed in the grey shaded areas is due to the filtering of the interfacing electronics. **e**, Coloured SEM images of the gDNP; uncoated (left), back coated with  $\sim 80$   $\mu\text{m}$  (middle) and with  $\sim 150$   $\mu\text{m}$  thick silk-fibroin (right) (scale bar=100  $\mu\text{m}$ ). **f**, Mechanical assessment: averaged compression force vs displacement for the gDNP coated with two SF thicknesses (coloured areas are standard deviations,  $n=10$  trials); the optical images correspond to two different conditions of the experiment. **g**, Functionality assessment: maximum normalized transconductance ( $g_m/V$ ) values and averaged  $V_{RMS}$  electronic noise level, of all gSGFET on a device measured in a PBS solution, inserted and measured in agarose gel brain model, and measured in the PBS solution after removal from agarose gel. **h**, Image sequence of a SF-coated gDNP at different time points during degradation in 0.6% agarose gel brain model.

**Awake *in vivo* full bandwidth recording with gDNPs.** We assessed full bandwidth recording capability by implanting a gDNP into awake, head-fixed mice. The electrophysiological signal measured by the graphene transistors was acquired with a g.RAPHENE system (g.tec medical engineering GmbH) that enables simultaneous recording in two frequency bands with different gains preventing amplifier saturation (Fig. 2a, Methods). gDNPs were implanted in the right hemisphere visual cortex (V1) and lowered until the tip reached hippocampal tissue. Baseline activity was recorded for (10-20 min). To induce network discharges and synchronicity of neuronal bursting 200nl of 4-AP (50mM), a selective blocker of Kv1 potassium channels<sup>28,29</sup> was focally injected into cortex adjacent to the gDNP (Fig. 2b).



137  
138  
139 **Fig. 2 Validation of *in vivo* full bandwidth recording capabilities of gDNPs.** **a**, Schematic of the recording setup and concept of a graphene transistor as a transducer  
140 for neural recording. **b**, Schematic of a mouse skull with location on the brain of the gDNP, the glass micropipette and the needle to inject the chemoconvulsant  
141 drugs. Right, coronal view of the mouse brain with the localisation of the gDNP. **c**, Long electrophysiological recording (120 mins) of two channels on the gDNP array  
142 (top: visual cortex, bottom: hippocampus). The full bandwidth ( $f > 0.001$  Hz, black) signal and the HP filtered signal  $>0.5$  Hz (dark red). Baseline activity, pin-prick SD,  
143 increased neuronal activity after 4-AP injection and seizures, some of them followed by a post-ictal SD. Below, different events in higher resolution: baseline (yellow)  
144 revealing theta activity in the lowest channel; profile visualization with recording from all 14 transistors following pinprick SD (beige); seizure activity shown for the  
145 uppermost and lowest channels of the gDNP (green). **d**, The recording shows the full bandwidth epileptiform activity followed by an SD event from all 14 transistors  
146 (black). The superimposed green recording corresponds to the signal measured with the glass micropipette. The subfigure shows the low frequency cross-correlation  
147 ( $< 5$  Hz), between the micro-pipette and all transistors on the shank. **e**, Averaged PSD over the electrophysiological recordings of all transistors during baseline,  
148 epileptiform activity, same activity HP filtered at 0.5 Hz (purple dashed-line) and post-mortem. The grey area highlights the low frequency part ( $<0.5$  Hz) usually cut-  
149 off with conventional AC-coupled recordings. **f**, Comparison of a baseline activity (black) and a post-mortem (blue) in one channel of the gDNP (top: full band, bottom:  
150 HP  $>200$  Hz). Lowest plot shows SNR evaluation for 4 *in vivo* experiments performed with 4 different gDNPs. The SNR is calculated for different bands (LFP: 1-70 Hz,  
high frequency: 80-200 Hz and very high frequency: 200-4000 Hz) and is the averaged SNR for all channels on each gDNP.

151 **Full bandwidth recordings.** Fig. 2c displays 2 hours of an electrophysiological recording session (only the uppermost and the lowest  
152 channels of the implanted gDNP displayed); the complete data set is shown in Supplementary Fig. S6. The ability of the graphene  
153 transistors to have long and stable full-bandwidth recordings without the need for electronic off-set readjustments contrasts to the  
154 limitation of DC-coupled passive electrodes<sup>30</sup>. The black lines correspond to the full bandwidth signal (HP > 0.001 Hz) and the red  
155 lines to the signal high-pass filtered above 0.5 Hz (which is the expected signal recorded by AC-coupled electrodes)<sup>31</sup>. The coloured  
156 regions correspond to different experimental conditions during the recording: baseline (yellow), needle-induced pin-prick SD<sup>32</sup> (pink),  
157 interictal activity<sup>14</sup> (orange) induced by chemoconvulsant drugs, and seizures (green & see Supplementary Fig. S7). During baseline  
158 recording in Fig. 2c, lower channels exhibit theta activity, correlated with animal movement, indicating that the gDNP reached the  
159 hippocampus, confirmed post-hoc by histological analysis of fixed brain sections (see Supplementary Fig. S8). After injection of 4-  
160 AP epileptiform spiking evolved and five seizures (over 60 minutes) were elicited in this example, one of which was followed by a  
161 post-ictal SD. A second cortical injection of 4-AP induced two additional seizures both followed by post-ictal SDs that were detected  
162 first in the hippocampus. In 5 different mice injected with 4-AP, an average number of  $7 \pm 3$  seizures were recorded in 60 min post  
163 drug injection. In this chemoconvulsant model SDs could be observed initially either in superficial cortical layers or, the hippocampus  
164 (Fig. 2c).

165  
166 **Validation of infraslow activity recordings with glass micropipette.** The fidelity of recorded ISA activity was validated by  
167 simultaneous recordings using a solution-filled glass micropipette, which is considered the gold-standard for ISA recordings. Fig. 2d  
168 shows the full bandwidth recording obtained with the gDNP (black lines) and the micropipette (green line) after injection of 4-AP.  
169 Both recordings reveal DC shifts preceding the seizure and a high amplitude ISA occurring after the seizure. The ISA deflection  
170 measured by the gDNP has a similar shape, magnitude and temporal duration as the signal recorded by the glass micropipette. A cross-  
171 correlation analysis (signal filtered <5 Hz) of the signal recorded by the glass micropipette and the 14 gDNP transistors demonstrates  
172 a very high correlation (above 90%) for ch03 and ch04 located at the same cortical depth as the micropipette.

173 **Assessment of the detection limits of gDNP.** Post-mortem recordings were acquired to characterize the electrical noise level of the  
174 gDNP in the activity-free brain state and, consequently, to quantify the detection limit of the gDNP. Fig. 2e shows the averaged power  
175 spectral density (PSD) calculated using the recordings of all channels in a gDNP, obtained from different brain states (baseline, after  
176 injection of 4-AP, and post-mortem). Compared to the baseline PSD, the large amplitude of the PSD at low frequencies (< 1 Hz) after  
177 4-AP injection is an indication of the interictal and infraslow activity in the brain. The dash-dot line in Fig. 2e corresponds to the  
178 activity recorded after injection of 4-AP, but with a typical HP filter of 0.5Hz, found in many AC-coupled recording systems, thus  
179 revealing the loss of ISA signal (grey area). In order to assess the detection limit in the conventional frequency bands (>1Hz), the  
180 recordings of the baseline were directly compared with post-mortem recordings. For instance, applying a digital filter (> 200 Hz) and  
181 comparing post-mortem with baseline validates the ability of gDNP to record spontaneous high-frequency activity (> 200 Hz) arising  
182 from groups of neurons in a non-pathological brain state. Beyond this qualitative comparison, we have calculated the signal-to-noise  
183 ratio (SNR) in three different bands, 1-70Hz (red), 80-200Hz (green), and 200-4000 Hz (blue) for different gDNPs implanted in four  
184 animals. SNR is calculated as root-mean square (RMS) amplitude ratio of the baseline and post-mortem recordings, filtered in the  
185 three different bands (see Methods). These results show that the gDNPs are able to record typical electrophysiological signal  
186 bandwidths with SNR ratios higher than 1 dB.

187 **Interictal activity and HFOs.** Fig. 3a shows interictal activity and associated HFOs (>80 Hz)<sup>12,13</sup> recorded by three of the transistors  
188 of a gDNP, each located at a different depth in the mouse brain. Filtering between 80 – 600 Hz (red curves in Fig. 3a) reveals layer-  
189 specific bursting of HFOs and sharp wave ripples, during inter-ictal spikes with characteristic oscillations of 200-300 Hz and 400-600  
190 Hz in the cortical and hippocampal channels respectively<sup>33</sup> (Supplementary Fig. S9); entrained inter-ictal epileptiform activity was  
191 found in all channels before each seizure. Two different pro-convulsive drugs (4-AP or picrotoxin PTX) were used to induce and  
192 evaluate epileptic activity. Fig. 3b illustrates characteristic examples of sharp wave ripples and HFOs induced by 4-AP and by PTX  
193 recorded by the lowest channel of the gDNP (hippocampal CA1 region). The HFO and ripple traces shown in Fig. 3b exhibit high-  
194 frequency tones up to 600 Hz. The filtered traces (>200 Hz) are compared to the original traces (full-bandwidth) for verification of  
195 ripples. The advantage of the gDNPs to monitor concurrent infraslow and high-frequency activity, is illustrated in Fig. 3c, which  
196 shows a post-ictal spreading depression (SD) arising from the hippocampus. The layer-dependent silencing of the neural activity by  
197 the hippocampal SD is represented in Fig. 3d in terms of activity variation [%]. The right plot in Fig. 3d shows the layer-dependent  
198 amplitude of the SD and the following hyperpolarization along the vertical profile (Supplementary Fig. S10 and Methods), revealing  
199 that the silencing of the neural activity in the hippocampus is correlated with the amplitude and subsequent hyperpolarization wave of  
200 the SD. Silencing of neural activity in the hippocampus by the SD is visualized with more clarity in Fig. 3e, where the spectrograms  
201 for the upper and lowest channel are compared. Fig. 3f shows more details of the seizure event recorded at three different depths,  
202 from the visual cortex to the hippocampus, comparing the signal in full band (black curves), HP filtered >0.5Hz (red curves), and LP  
203 filtered < 0.5Hz (green curves).

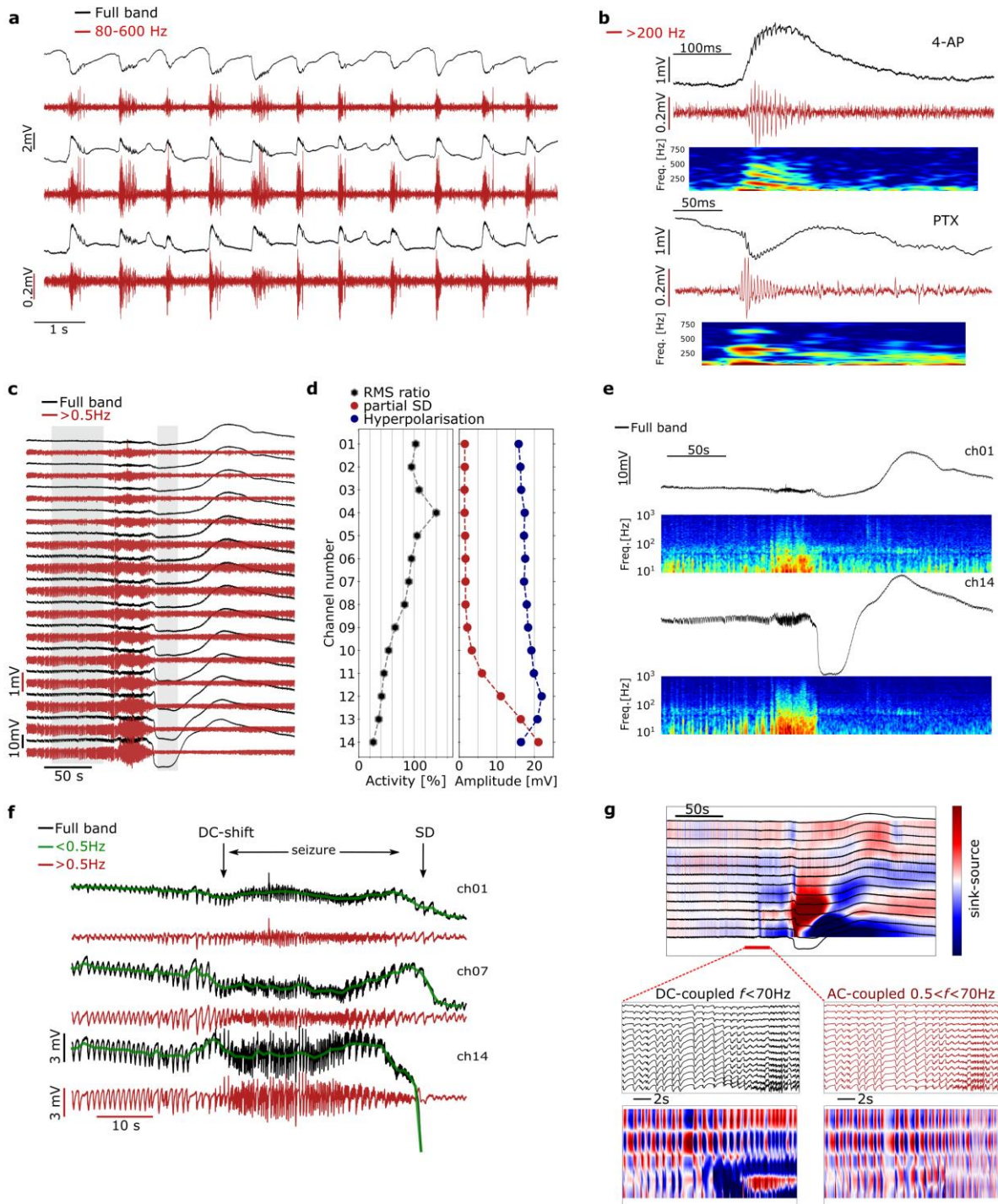


**Fig. 3 Electrophysiological recording of characteristic epilepsy biomarkers.** **a**, Interictal activity in three different channels of a gDNP (ch01, ch07, ch14) (red curves BPF 80 Hz – 600 Hz). **b**, Sharp-wave ripples and HFO recorded in the hippocampus induced by 4-AP and PTX (full band: black, HP>200 Hz: red); the figure also shows the corresponding spectrograms (range 10-800 Hz). **c**, Electrophysiological full band recordings (black curves) and HP filtered at 0.5 Hz (red curves) from the cortex (top channel) to hippocampus (bottom channel) illustrating a post-ictal spreading depression (SD) arising from the hippocampus after a seizure event. **d**, Neural activity variation (before seizure and during SD, grey area in (c)) and amplitudes of the SD and hyperpolarisation waves concurrent with the seizure across the vertical profile. Neural activity variation is calculated for each channel by comparing activity before and during the SD (grey shaded areas in panel (c)). **e**, Hippocampal neural silencing during the SD is illustrated by the spectrograms (range 10-1000 Hz) of the uppermost and lowest channels of the gDNP (ch01, ch14). **f**, Three channels (ch01, ch07, ch14) showing full band recording (black) and band-pass filtered (> 0.5 Hz, red) of a seizure followed by a hippocampal SD; in green the low-freq. component of the recording (< 0.5 Hz) overlapped to the full bandwidth signal, showing an ictal DC shift associated with a seizure, and followed by the SD. **g**, Current-source density (CSD) analysis of the low frequency activity (< 70 Hz), showing source and sinks in the hippocampus during the SD. Below: blow up of the pre-ictal to seizure transition (< 70 Hz), showing dipoles in the different layers of the cortex and hippocampus. The two graphs correspond to the CSD analysis performed with (left) and without (right) the contribution of low frequency components.

204

205

206

207

208

209

210

211

212

213

214

215

216

217

218

219 **Current-source density analysis using infraslow activity.** Ictal DC shifts can be associated with seizures<sup>16,34</sup> but are usually removed  
220 from recordings due to the requirement for high-pass filtering applied to conventional AC-coupled electrodes<sup>31</sup>. We are able to record  
221 these using gDNPs and observe DC shifts immediately prior to seizure onset, with their amplitude (0.5-3mV) and polarity related to  
222 cortical layer (Fig. 3f). The inversion of DC shifts can be used to identify current sources and sinks through the cortical laminae.  
223 Current-source density (CSD) analysis is a technique to identify source activation in a variety of focal neurological disorders including  
224 epilepsy<sup>35</sup>. CSD analysis (see Methods) of the data in Fig. 3c reveals a large net ionic sink in the hippocampal extracellular space  
225 after the seizure, followed by a large source at the beginning of the hyperpolarization wave (Fig. 3g). Enlarging the seizure onset  
226 region, 4 sink and source regions are identified through the laminae profile. CSD analysis computed without the infraslow components  
227 (0.5Hz<f<70Hz) fails to report the ionic sinks preceding and during the seizure in the bottom layers (Fig. 3g, AC-coupled panel),  
228 illustrating the importance of using full-bandwidth recordings for CSD analysis to avoid misinterpretation of the extracellular potential  
229 sinks and sources (Supplementary Fig. S11 illustrates additional examples of CSD analyses).

231 **Chronic functional validation and biocompatibility assessment.** Finally, we discuss the stability and chronic functionality of  
232 gDNP, defined by the ability to maintain a suitable signal-to-noise ratio recording spontaneous epileptiform activity over time. We  
233 implanted gDNPs in the right-hemisphere somatosensory cortex of WAG-Rij rats (n=4), a rodent model of absence epilepsy<sup>36</sup>, and  
234 obtained chronic full-bandwidth recordings over a 10-week period Fig. 4a. WAG-Rij rats exhibit frequent spontaneous spike-and-  
235 wave discharges (SWDs), a characteristic thalamocortical oscillation between 8-10 Hz<sup>36</sup>. Implanted animals were connected 1-2 times  
236 per week for tethered recordings (using a commutator to enable free movement of the rats see Fig. 4a).

237 **Stability of implanted transistors.** Transistor curves were measured in each recording session to assess device stability, changes at the  
238 device/tissue interface and importantly, to permit selection of an optimal V<sub>gs</sub> to maximise SNR; a feature possible with active sensor  
239 devices<sup>19</sup>. Fig. 4b shows the averaged transfer curves of a gDNP measured over 10 weeks (see also Supplementary Fig. S12). The  
240 stability of the transistors' performance is illustrated in Fig. 4c, which depicts the position of the CNP and the maximum value of g<sub>m</sub>  
241 over the implantation period. The averaged g<sub>m</sub> value remains approximately constant over the whole study. Since g<sub>m</sub> is directly related  
242 to the tissue/graphene interfacial capacitance and to the carrier mobility in graphene, the g<sub>m</sub> stability strongly suggests little or no  
243 variation of these two parameters. CNP (Fig. 4c) shows a significant shift (200 mV) during the few first days after implantation, which  
244 then remains stable for the rest of the experiment. We tentatively attribute the initial shift to the adsorption of negatively charged  
245 species, which reduce the intrinsic p-type doping of the graphene transistors<sup>20</sup>.

246 **Long-term functionality of gDNPs.** Long-term functionality of the gDNP was assessed by evaluating the quality of the recorded  
247 signals over the implantation period using two parameters, normalized SWD power amplitude and the transistor noise (V<sub>RMS</sub>).  
248 Normalized SWD power amplitude is defined as the RMS (calculated in the frequency band 1-500 Hz) of the SWD activity normalized  
249 by the baseline activity (non-SWD periods, see inset of Fig. 4d and Supplementary Fig. S13). V<sub>RMS</sub> over time is extracted by averaging  
250 the RMS values at very high frequency (500-2000 Hz) in the non-SWDs periods of the recording, where we expect the power of  
251 neural activity to be closer to the transistor's noise (see Fig. 2f). For further details, refer to Methods and Fig. S12. In Fig. 4d the  
252 variation of these two parameters over time is shown, demonstrating the ability of the implanted devices to monitor seizure activity  
253 with high fidelity during the whole implantation period. The slight increase in the normalized SWD activity could result from a  
254 strengthened coupling between neural tissue and the gDNP or from an increase in the seizure power and duration as the animal ages<sup>37</sup>.

255 **Correlation between SWDs and infraslow activity.** The WAG Rij rat chronic model of absence epilepsy offers the possibility to  
256 investigate correlations between infraslow activity and SWD events. Because of the full-bandwidth capability of the gDNP, we were  
257 able to observe DC shifts (< 0.5 Hz) associated with SWDs, and a correlation between the amplitude and polarity of the DC shift with  
258 the depth of the neocortex layers. Fig. 4e shows the uppermost and lowest channel with opposite associated DC shifts during each  
259 SWDs. In this experiment we observed a positive DC shift (~1.5 mV) in the superficial layers L1, L2/L3, and L5 to a lesser degree,  
260 and a negative DC shift in the lowest cortical layers (Supplementary Fig. S14). The latter is not observed after application of a HP-  
261 filter (>0.5 Hz) as typically used with conventional AC-coupled microelectrodes (Fig. 4e, grey). The observed correlation between  
262 the SWDs and ISA, and layer-dependent polarity of the DC shift persist over the implantation period. Representative seizure events  
263 showing SWDs and DC shifts over time are shown in Fig. 4f.

264 We calculated the phase of the ISA (limited to the 0.01-0.1 Hz band) and the power of the neural activity associated to the SWDs (5-  
265 9 Hz). Fig. 4g displays one of the upper channels together with its spectrogram (range 1-14 Hz). The distribution of the ISA phase  
266 with the power amplitude of the SWDs is plotted for each channel (Fig. 4h), showing a clear inversion in the lower layer of the  
267 neocortex (see Methods and Supplementary Fig. S15). This correlation between ISA and SWD was also observed in the other  
268 implanted WAG-Rij rats (n=4, Supplementary Fig. S16). gDNPs are therefore a promising electrophysiology tool to gain further  
269 understanding of the influence of thalamocortical oscillations in SWD generation<sup>38</sup>.

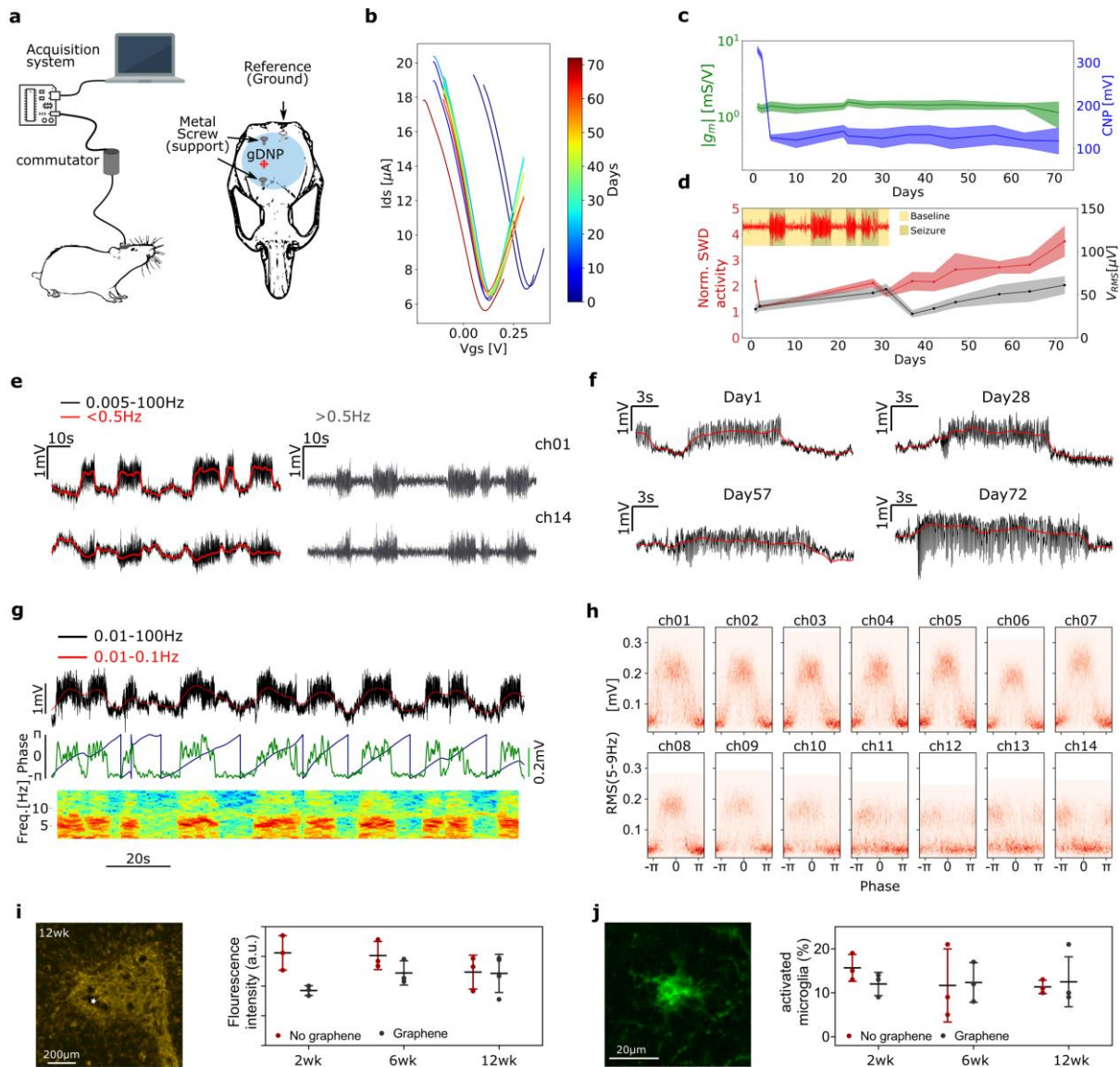


**Fig. 4 Chronic assessment of stability, functionality and biocompatibility of gDNPs.** **a**, Left: Cartoon of a WAG-Rij rat tethered via a commutator and the electronics for the data acquisition. Right: Schematic of the rat skull with the approximate location of the gDNP. **b-d**, Stability and quality of the recordings. **b**, Averaged transfer curves of all transistors of the gDNP over the implantation time. **c**, Averaged values of the maximum transconductance  $g_m$  (green) and the charge neutrality point (CNP, blue) of the transistors transfer curves. **d**, Normalized SWD activity over implantation time, calculated as the ratio of the SWD activity and baseline activity. Inset: example of SWDs events (red), highlighting the periods considered baseline and SWD. The graph also shows the average  $V_{RMS}$  noise (black) of all channels over the implantation period. **e**, SWD in the uppermost and lowest channels of the gDNP; ISA component (red < 0.5 Hz) overlapped to the 0.005-100 Hz signal (black); in grey the same signal filtered above 0.5 Hz. **f**, Illustrative SWD events measured by the same channel at days 1, 28, 57, and 72. **g**, Typical recording of one of the transistors located in the rat cortex showing SWDs events concurrent with ISA. Phase of the ISA (blue) and power of the SWD activity (green). The spectrogram (range 1-14 Hz) shows the increase in power during the SWDs. **h**, Density distribution for all channels evaluated in a long recording (1600s). y-axes correspond to the RMS (5-9 Hz) associated with the SWD and the x-axes represent the phase of the ISA (red represents higher density); shows a clear correlation between ISA phase and SWD power with a phase inversion in the deeper cortex layers. **i-j**, Chronic biocompatibility assessment of SF-coated gDNPs implanted in Sprague-Dawley rats ( $n=20$ ) by monitoring inflammatory markers. **i**, Fluorescent image of GFAP, as a measure of positive astrocyte cells, in the area of insertion at 12 weeks post implantation (the star mark shows the insertion point). Time evolution (2, 6, 12 weeks) of the fluorescence intensity (calculated at  $150\mu\text{m}$  from the probe sites) obtained for flexible gDNP with graphene (grey), and gDNP without graphene (red). **j**, Example of microglial activation (fluorescence image). Time evolution (2, 6, 12 weeks) of activated microglia in the vicinity of the implanted probes (in an area of  $0.7\text{mm}^2$ ) obtained for the two types of probes (graphene, no-graphene).

**Chronic biocompatibility of implanted gDNP.** In addition to the chronic functional validation of the gDNP, we conducted an extensive chronic biocompatibility study to assess any potential neuro-inflammation caused by the invasive nature of the penetrating neural probes, the presence of CVD graphene, or by the release of SF following implantation. gDNPs with or without graphene at the recording sites were implanted in adult, male Sprague-Dawley rats ( $n=20$ ). Histological and immunohistochemical studies were conducted at 2, 6, and 12 weeks' post-implantation and compared to the contralateral hemisphere, without device implantation (see Methods and Supplementary Fig. S17, Fig. S18). Fig. 4i shows a fluorescence image of GFAP immunostaining (positive marker for astrocyte cells) in the area of insertion 12 weeks post implantation (brain sections at  $800\mu\text{m}$  from pia). There is no significant increase in the presence of astrocyte cells (typically associated with inflammation) in the area directly surrounding the probe site, when the



299 “graphene” gDNP is compared with the “no-graphene” gDNP (Fig. 4i, right graph). Moreover, no significant difference was observed  
300 at 2, 6, and 12 weeks’ post-implantation. Further, the microglial activation state, assessed by morphological analysis of cells stained  
301 for ionized calcium binding adaptor molecule 1 (Iba-1), showed no significant increase in the abundance of activated microglia present  
302 in the area surrounding the implantation site (Fig. 4j). Additional immunohistochemical analysis showed no sign of an inflammatory  
303 response over the 12-week period for either device used (Supplementary Fig. S17). Altogether, the chronic biocompatibility study  
304 indicates that gDNPs are suitable for chronic implantation, inducing no significant damage nor neuroinflammatory response.  
305

## 306 Outlook

307 In this work, we demonstrate the capability of flexible depth neural probes based on linear arrays of graphene microtransistors to map  
308 the entire frequency bandwidth, simultaneously recording infraslow activity and high frequency neural oscillations through the cortex  
309 laminae to upper hippocampal layers. Measuring the full bandwidth of neuronal activity in the brain with high spatiotemporal  
310 resolution will advance our understanding of the brain, in health and disease. While SD and seizures can occur concurrently, the inter-  
311 layer dynamics and the effect of SD on epileptic activity across the cortical laminae and deeper regions of the brain remain largely  
312 unknown. gDNPs allowed us to reveal associations between infraslow activity (including spreading depolarizations<sup>17,39</sup> and small pre-  
313 seizure DC shifts<sup>15,16,40</sup>) and higher frequency activity (including SWDs<sup>38</sup> and HFOs<sup>12,13</sup>) in rodent models of drug-induced seizures  
314 and chronic epilepsy<sup>36</sup>. Together with validation of chronic functionality of implanted gDNPs and their biocompatibility, this work  
315 underlines very distinct advantages of this technology for *in vivo* epilepsy preclinical research. We envision that uptake of this  
316 technology will aid mechanistic understanding of seizure initiation and termination and gain insight into the nature of post-seizure  
317 spreading depolarisations, recently implicated in sudden unexplained death in epilepsy (SUDEP)<sup>41,42</sup>. Clinical development could  
318 result in depth probes capable of simultaneous high-quality wide-band (DC to HFO) recordings, from multiple brain regions, during  
319 pre-surgical monitoring improving identification of seizure onset zones (SOZ) and ultimately surgical outcome<sup>14</sup>. Beyond epilepsy  
320 research, this technology is expected to advance our understanding of neurological diseases and could easily be applied to study  
321 disorders associated with infraslow activity including traumatic brain injury, stroke and migraine<sup>2</sup>.  
322

## 323 Methods

324 **Graphene growth, transfer and characterization.** Graphene was grown by chemical vapor deposition (CVD) on copper foil (Alfa  
325 Aesar Coated). Prior to growth, copper foil was electropolished for 5 min in a H<sub>2</sub>O (1 L) + H<sub>3</sub>PO<sub>4</sub> (0.5 L) + ethanol (0.5 L) +  
326 isopropanol (0.1 L) and urea (10 g) solution<sup>43</sup>. The CVD reactor consists of a tubular three zone oven with a quartz tube (1600x60  
327 mm). After loading Cu foil, an annealing step (1h) was performed, prior to growth, at 1015°C under a 400 sccm Argon flow at 100  
328 mbar. This was followed by the growth step (15 min growth step), at 12 mbar under a gas mix of 1000 sccm Argon, 200 sccm  
329 hydrogen, and 2 sccm methane. Transfer of the graphene from copper foil to polyimide was achieved using a wet-etching chemical  
330 method. A supporting poly(methyl methacrylate) PMMA 950K A4 was spin-coated on the graphene/copper foil and left to dry for 12  
331 h. Back side graphene is removed with a 10% HNO<sub>3</sub> solution. Subsequently, the sample was laid on the etchant solution composed of  
332 FeCl<sub>3</sub>/HCl (0.5M/2M) to remove copper for at least 6 h. Next the graphene/PMMA stack was rinsed in DI water multiple times before  
333 transfer onto the polyimide-coated wafer. The wafer was dried for 30 min at 40 °C on a hot plate, and annealed in a vacuum hotplate  
334 by increasing the temperature gradually up to 180 °C. Finally, the PMMA was removed in acetone and isopropanol. CVD-grown  
335 graphene was characterized by Raman spectroscopy using a Witec spectrograph equipped with a 488 nm laser excitation line. To  
336 assess the quality of the graphene film (see Supplementary Fig. S1) Raman maps of 30 x 30 μm<sup>2</sup> (with 1 μm resolution) were acquired  
337 using a 50x objective and the 600 g nm<sup>-1</sup> grating; laser power was kept below 1.5 mW to avoid sample heating.  
338

339 **Microfabrication of flexible gDNPs.** Flexible neural probes were fabricated using standard microelectronic fabrication technology  
340 on a rigid 4-inch sacrificial Si/SiO<sub>2</sub> wafer. A 10 μm thick polyimide (PI-2611, HD MicroSystems) layer was spin-coated and cured  
341 at 350 °C in a N<sub>2</sub> atmosphere. To reduce the shank width of the depth neural probes, we used a two-metal level strategy in which the  
342 metal tracks, separated by PI, are interconnected by via-holes. After evaporation and definition (via lift-off) of a first metal layer of  
343 Ti/Au (10/100 nm), a 3 μm-thick PI layer was spin-coated and cured. A protective mask of Al (200nm) was used to etch the second  
344 PI layer by oxygen plasma and form the via-holes. On top of the via-holes a second metal layer of Ti/Au (10/100 nm) was applied to  
345 interconnect the two metal layers. CVD graphene was transferred onto the patterned wafer as described in the section above. After  
346 removing the PMMA protection layer, the graphene active areas were defined by means of an oxygen-based reactive ion etching. A  
347 sandwich-like contact strategy was used to improve the contact at the drain and source terminals; the used top metal structure was  
348 Ni/Au (20/200nm). For passivation, a 2μm-thick chemically resistant polymer is deposited (SU8-2005 MicroChem) with open  
349 windows in the channel region. Finally, the gDNP structure was defined in a deep reactive ion etching process using the thick AZ9260  
350 positive photoresist (Clariant) as an etching mask. The polyimide probes were then released from the SiO<sub>2</sub> wafer and placed in a zero  
351 insertion force connector in order to interface our custom electronics.  
352

353 **Characterization of gDNPs in saline.** The graphene SGFETs on the neural probes were characterized in PBS solution (150mM).  
354 Drain to source currents (I<sub>ds</sub>) were measured varying the gate-source voltage (V<sub>gs</sub>), versus a Ag/AgCl reference electrode which was  
355 set to ground. Steady state was ensured by acquiring the current only after its time derivative was below a threshold (10<sup>-7</sup> A s<sup>-1</sup>). The  
356 detection limit of the graphene SGFET were assessed by measuring the power spectral density of the DC current at each polarization

point V<sub>gs</sub>. Integrating the PSD over the frequencies of interest (1Hz-2kHz) and using the transconductance allowed us to calculate the root-mean-square gate voltage noise V<sub>RMS</sub>. The noise measurement was performed in a Faraday cage, with DC-batteries powering the amplifiers, in order to reduce any 50 Hz coupling or pick-up noise. Additionally, the frequency response of the device's transconductance was measured by applying a sum of sinusoidal signals at the electrolyte solution through the reference electrode and by measuring the modulation of the drain current. The acquired signals were split into two bands, low frequencies ( $\approx$  0–10 Hz), at which drain–source current was simultaneously acquired for all transistors in an array, and higher frequencies (10 Hz–30 kHz), at which each transistor was recorded individually.

**Back coating of gDNP with silk fibroin.** Temporary stiffening of the gDNPs with silk-fibroin is achieved using a micro-structured PDMS mould with the shape of the neural probes. To fabricate the moulds, PDMS is cast on a standard 4-inch silicon wafer with pre-patterned 100  $\mu$ m and 200  $\mu$ m thick SU8 (SU8-2050) epoxy resin. The back-coating procedure is as follows: first, the probe is placed in the mould trench filled previously with water, with the transistor side facing down. Through surface tension the probe self-aligns in the mould. After evaporation of the water, silk fibroin (Sigma Aldrich, Silk, Fibroin Solution 50 mg/mL) was applied via a syringe to the mould's trench. We double coat the shank in drying intervals of 20 minutes and then slowly increase the temperature on a hotplate to 80 °C, leaving the SF curing for 1h 30 minutes. By increasing the duration of the water annealing step we managed to have a delayed dissolution time compared to SF cured at room temperature. After curing, the coated probe can be easily removed from the PDMS mould (see Supplementary Fig. S3). In all presented *in vivo* experiments we implanted the flexible gDNPs with a 150  $\mu$ m thick SF back-coating.

**Assessment of mechanical properties of the stiffened gDNPs.** Standard compression tests against a hard silicon (Si) substrate were performed to assess the mechanical properties of our SF-coated probes. Buckling experiments were carried out in a UMIS nanoindenter from Fischer-Cripps Laboratories. A custom clamp was fabricated to fix the probes at the end of the indenter shaft that, in turn, was connected to the actuator and load cell. Buckling tests were carried out at a loading rate of 8.8 mN/s. Once the indenter detected noticeable buckling the test was automatically stopped. The maximum applied load that the indenter can apply is 500 mN. Applied force vs displacement was measured until the probe started buckling and eventually broke down. We additionally measured the Young's modulus of the SF cured at 80 °C by means of nano-indentation tests. SF was drop casted on a 2x2cm<sup>2</sup> Si chip and cured. The indentation measurements were performed using a NHT2 Nanoindentation Tester from Anton-Paar equipped with a Berkovich pyramidal-shaped diamond tip. A maximum applied load of 5 mN was applied with a loading segment of 30 s followed by a load holding segment of 10 s and an unloading segment of 30 s. The hardness and reduced Young's modulus are reported as an average value of at least twenty indentations, performed on top of each sample (in the central region). Young's modulus values in the range of 10 GPa were measured for 80 °C cured SF (see Supplementary Fig. S4).

**Electronics for *in vivo* recordings with gDNPs.** The experimental setup used to perform the *in vivo* recordings provides V<sub>s</sub> and V<sub>d</sub> bias control and current-to-voltage conversion for up to 16 channels (g.RAPHENE, g.tec medical engineering GmbH, Austria). The instrumentation splits the recorded signals into two bands with different gains: low-pass filtered (LPF, < 0.16 Hz, 10<sup>4</sup> gain) and band-pass filtered (BPF, 0.16 Hz < f < 160 kHz, 10<sup>6</sup> gain). Two custom Simulink models were used: i) to perform the transfer curve of the microtransistors once inserted and at the end of the experiment; ii) to set the V<sub>s</sub> and V<sub>d</sub> bias and acquire the recorded signals. Signals were sampled at 9.6 kHz and at 19kHz depending on the type of experiment (see Supplementary Table1).

**Ethical approval and animal handling for acute and chronic experiments.** Animal experiments were conducted in accordance with the United Kingdom Animal (Scientific Procedures) Act 1986, and approved by the Home Office (license PPL70-13691). C57BL/ mice were bred (2-4 month old males), while WAG rats were imported (Charles river, used 6-9 months of age). Animals were housed on 12 h/12 h dark/light cycle, and food and water were given *ad libitum*. Prior to headbar surgery, animals were group housed, but after this, animals were individually housed.

**Acute preparation surgeries for headbar attachment and craniotomy.** For both surgeries, aseptic techniques were used with mice anaesthetized using isoflurane (988-3245, Henry Schein, U.S.A.) and placed in a stereotaxic frame (David Kopf Instruments Ltd., U.S.A.). Viscotears applied (Bausch + Lomb, U.S.A.) and pain relief, which consisted of sub-cutaneous Buprenorphine (0.5 mg / Kg; Ceva, France) and Metacam (15 mg /Kg; Boehringer Ingelheim, Germany), were injected. Saline was administered just before recovery or every 45 mins depending on the length of surgery. To apply the headbars for the Neurotar system the skin on the top of the head was cut to expose the skull. The skull was cleaned and dried, which enabled drilling (RA1 008, Henry Schein, U.S.A.) of a small hole in the left hand visual cortex for a metal support screw (00-96X3-32, Plastics One, U.S.A.). Using vetbond (1469SB, 3M, U.S.A.), the headplate (Model 9, Neurotar, Finland) was firmly attached and strengthened using dental cement before Kwik-cast (KWIK-CAST, W.P.I., U.K.) covered the exposed skull. Mice were checked daily to ensure recovery. After at least 5-days of recovery, habituation was performed by placing the mouse in the Neurotar frame for increasing periods of time (15-60 mins) over several days. On the day of recording, a craniotomy was performed. Under Isoflurane anaesthesia, with administration of pain medication and intramuscular Dexamethasone (1 mg / Kg; intra-muscular; 7247104; MSD Animal Health, U.S.A.), two areas were exposed. A large (2x2mm) craniotomy over somatosensory and visual cortex on the right-hand side and a small drill hole over the motor cortex on the left hand side. Cold Cortex buffered saline was continually applied to the craniotomies. After completion, exposed dura was covered with Cortex buffered saline, sterilised slygard (~200  $\mu$ m thickness), and a kwik-cast layer. After ~2-hours post-recovery, the animal

417 was moved to the Neurotar frame and the craniotomies were exposed by removal of the kwickcast and sylguard. The gDNP was  
418 carefully connected to a PCB and lowered using a micromanipulator to just above the dura over the visual cortex. The dura was gently  
419 pierced using either micro-dissection scissors or a 26-gauge needle and gDNP lowered ~2 mm into the brain. A reference wire  
420 (Ag/AgCl<sub>2</sub>) was placed in the ipsilateral motor cortex and g.tec hardware (see *Electronics for in vivo recordings with gDNPs*) used to  
421 perform a DC characterisation curve to determine the optimal V<sub>gs</sub> and initiate recordings. Chemoconvulsant was injected into the  
422 brain using a Nanofil injection system (W.P.I., U.K.). At the end of the experiment, sodium pentobarbital was administered intra-  
423 peritoneally.  
424

**Recording with solution-filled glass micropipette.** Borosilicate capillary tubes (OD: 1.50mm, ID: 0.86mm, Warner Instruments)  
425 were pulled using a horizontal puller (Sutter instruments P-97, resistance of 3-5 MOhm) and filled with artificial Cerebral Spinal Fluid  
426 (NaCl: 119mM, KCl: 2.5mM, CaCl<sub>2</sub>: 2.5mM, MgSO<sub>4</sub>: 1.3mM, NaH<sub>2</sub>PO<sub>4</sub>: 1.25mM, NaHCO<sub>3</sub>: 25mM, Glucose: 10mM) and attached  
427 to an Axon instruments CV-7B head stage. A micro-manipulator (MM3301, WPI) was used to position the pipette above the cortical  
428 surface before insertion approximately 400µm into the cortex. The head-stage was provided with the same reference as the gDNP, a  
429 chlorinated silver wire touching the ipsilateral motor cortex. The headstage was connected to a Multiclamp 700B amplifier (Axon  
430 Instruments) operating in current clamp mode. Analogue-Digital Conversion and TTL pulse delivery for temporal synchronisation  
431 was achieved using the Micro1401 MkII (CED, Cambridge, U.K.). Data was acquired using WINEDR sampling at 20 kHz with a 4  
432 kHz Bessel filter.  
433  
434

**Chronic preparation surgery and recording.** First, the gDNP was fibroin coated, as described above, to aid insertion. The rat was  
435 anaesthetised to a surgical depth using Isoflurane. After placement in a stereotaxic frame, Viscotears were applied and pain medication,  
436 which consisted of Bupenorphine (0.15 mg / Kg; sub-cutaneous; Ceva, France) and Metacam (4.5 mg /Kg; sub-cutaneous; Boehringer  
437 Ingelheim, Germany), was applied. The skull was cleaned and dried. Small burr holes (~1 mm) were drilled at four positions: 1)  
438 Somatosensory cortex for gDNP (since the perioral somatosensory cortex is the focal area for SWDs<sup>44</sup>); 2) contralateral cerebellum  
439 for a reference Ag/AgCl wire held in place by a nylon screw; 3) Motor cortex, ipsilateral, for a support screw; and 4) Visual cortex,  
440 ipsilateral, for a support screw. The metal screws were inserted and provided structural support for the dental cement. Next, the gDNP  
441 and the reference wire were inserted, and a DC characterisation curve confirmed that the transistors were performing optimally. Dental  
442 cement, mixed with vetbond, was applied around the PCB for support. Animals were weighed daily and their physiology was  
443 monitored to ensure a full recovery. For recording, animals were anaesthesia-free and moving, with the PCB-interface on the head  
444 connected to an Omnetics cable (A79635, Omnetics, U.S.A.) that interfaced with the g.tec recording hardware as described above.  
445 After ~5-minutes for settling, a DC characterisation curve was recorded to allow accurate calibration of the gSGFETs. A script  
446 calculated the optimal V<sub>gs</sub> based on the transfer curves. Recordings were performed for ~10-60 minutes twice a week for 10 weeks.  
447 After recording, the Omnetics wire was disconnected and a protective cap was applied.  
448  
449

**Data analysis.** All electrophysiological data were analysed using Python 3.7 packages (Matplotlib, Numpy, Neo and Elephant) and  
450 the custom library PhyREC (<https://github.com/aguimera/PhyREC>). The conversion of the recorded current signals (LPF and BPF)  
451 to a voltage signal was performed by summation of the two signals and interpolation in the in vivo/chronic measured transfer curve  
452 of the corresponding gSGFET. The transfer curves were always measured at the beginning and end of every recording to ensure that  
453 no significant variations were present and to detect any malfunctioning transistor. Moreover, all recordings presented in the manuscript  
454 have been calibrated with the nearest-recorded transfer curve to ensure high fidelity in the voltage-converted signals. The SNR shown  
455 in Fig. 2f was evaluated by the ratio of the RMS mean value over 25s of recording of baseline (spontaneous activity) and post-mortem  
456 (no activity). The signal is BP filtered in three different bands corresponding to the LFP activity (1-70 Hz), high frequency (80-200  
457 Hz) and very high frequency activity (200-4000 Hz). RMS values were calculated with a sliding window of 500ms for the 1-70 Hz  
458 band and with a sliding window of 10ms for the other two bands. For each BP filtered signal the mean RMS ratio is calculated and  
459 averaged for all 14 channels in the gDNP. SNR for the different bands is evaluated from a total of 4 in-vivo experiments with 4  
460 different gDNPs (Fig. 2f). SNR is expressed in dB ( $20 \cdot \ln(RMS(S)/RMS(N))$ ). The silencing of neuronal activity shown in Fig. 3d, was  
461 extracted using the AC-coupled recording (HP >0.5 Hz). Then the RMS values of the pre-ictal phase (calculated with a sliding window  
462 of 1s) are averaged over 50s time. Similar analysis was performed for the time during the SD (15s, shaded areas in Fig. 3d). The ratio  
463 of the two averaged RMS values corresponds to the neuronal activity variation [%] (before and during the SD). The amplitude of the  
464 hippocampal SD and hyperpolarization wave in Fig. 3d, is evaluated using the recording LP filtered in the infra-slow regime (<0.5  
465 Hz) and re-sampled at 3 Hz (instead of 9.6 kHz used in the original recording). The zero of the voltage was set using the mean value  
466 of the signal 50s before the pre-ictal phase (see Supplementary Fig. S10), the minimum and maximum values for each channel were  
467 extracted (corresponding to the SD and the hyperpolarisation amplitude respectively). Current source density analysis applied to the  
468 low-frequency part of the potential (LFP), was calculated with the python open source Elephant library (Elephant electrophysiology  
469 analysis toolkit) using the class “Current Source Density analysis (CSD)” and the method 1D – StandardCSD was chosen for the  
470 linear gDNP array. A homogeneous conductivity of the neural tissue of  $\sigma=0.3$  S/m across the different layers was used for the  
471 calculations. The ISA concurrency with the SWD shown in the histogram in Fig. 4h was evaluated by performing the Hilbert transform  
472 to extract the phase of the ISA (0.01-0.1 Hz) and the RMS between 5-9 Hz (typical bandwidth for the SWD). Supplementary Fig. S15  
473 shows in more detail the dependency of ISA phase and SWD amplitude.  
474

475  
476

## Chronic biocompatibility study

477 **Device manufacture and sterilization.** Two types of flexible gDNP were fabricated for the immunohistochemical study: One with  
478 graphene and one without graphene following the fabrication steps described above section (*Fabrication of gDNPs*). In the devices  
479 gDNP without graphene the graphene instead of being defined by RIE, was etched away. By doing so, we make sure that all the  
480 fabrication steps are equal for both, gDNP with and gDNP without graphene. For comparison to rigid devices currently available on  
481 the market, iridium Neuronexus electrodes (A1x32-Poly2-5mm-50s-177) with a thickness of 15µm and length 5mm were implanted.  
482 Devices were sterilised individually with ethylene oxide, using an Anprolene AN-74i sterilizer, performed according to manufacturer's  
483 instructions.

484 **Surgical implantation of devices.** Adult male Sprague-Dawley rats (230-280g) were used for this study (Charles River, England).  
485 All animals were kept in individually ventilated cages (Techniplast, GR1800) in groups of 3-4, housed at a constant ambient  
486 temperature of  $21 \pm 2^\circ\text{C}$  and humidity of 40–50%, on a 12-h light, 12-h dark cycle. All rats were given free access to diet and water.  
487 Experimental procedures were conducted in compliance with the Animal welfare act 1998, with approval of the Home Office and  
488 local animal welfare ethical review body (AWERB). Animals were anaesthetized with Isoflurane (2-3%) throughout surgery, and  
489 depth of anaesthesia was monitored with the toe pinch reflex test. Animals were fixed to a stereotaxic frame (Kopf, model 900LS),  
490 and body temperature was maintained with a thermal blanket. A small craniotomy (~3mm) was made with a micro drill (WPI,  
491 OmniDrill35) above the somatosensory cortex, the dura was excised and one of three depth probe devices were implanted; i) graphene  
492 device, ii) no graphene device, or iii) Neuronexus device, at coordinates relative to bregma; anteroposterior (AP): 0mm, dorsoventral  
493 (DV): +3.5mm, and mediolateral: -1.5mm. The craniotomy site was sealed with Kwik Sil (WPI), secured with dental cement, the skin  
494 was sutured closed, and anaesthetic was withdrawn, with saline (20ml/kg) and buprenorphine (0.03mg/kg in saline) given  
495 subcutaneously to replace lost fluids and reduce post-operative pain.

496 **Tissue collection and processing.** Animals were culled at 2, 6 or 12 weeks' post-implantation dependent on the analysis to be performed.  
497 Tissue was taken either for immunohistochemical analysis of cells related to inflammatory processes, or for cytokine analysis of  
498 inflammatory markers. For a further description of the techniques used, and analysis see Supplementary Information.

499 **Histology.** Animals were perfused with 4% PFA to fix tissue. Axial plane brain sections were cut at 50µm thickness with a vibrotome  
500 (Leica, VT1200). Sections at an approximate electrode site depth of 0.8mm were selected for staining. Sections were stained free-  
501 floating for two markers; i) ionized calcium binding adaptor molecule 1 (Iba1) to quantify microglial population, or ii) Glial fibrillary  
502 acidic protein (GFAP) staining to assess astrocyte presence (see Supplementary Methods for details of immunohistochemistry). Slides  
503 were imaged with a Leica SP8 confocal microscope with a 10x objective lens. Laser power and digital gain was kept consistent across  
504 imaging sessions. A single optical section of the tissue surrounding the probe site was taken within the middle portion of the section  
505 as to avoid edge effects. Details of the analysis of histology is provided in Supplementary Methods section.

506 **Enzyme-Linked ImmunoSorbent Assay (ELISA) Protocol.** For ELISA, animals were culled by rising concentration of CO<sub>2</sub>. Brain  
507 tissue was extracted, snap frozen in liquid nitrogen, and stored at -80 °C until further use. Brain tissue was lysed by addition of NP-  
508 40 lysis buffer (150 mM NaCl, 50 mM Tris-Cl, 1% Nonidet P40 substitute, Fluka, pH adjusted to 7.4) containing protease and  
509 phosphatase inhibitor (Halt™ Protease and Phosphatase Inhibitor Cocktail, ThermoFisher Scientific) followed by mechanical  
510 disruption of the tissue (TissueLyser LT, Qiagen). Samples were centrifuged at 5000RPM for 10 minutes, and the supernatant stored  
511 at 4 °C until further use. A bead-based multiplex ELISA kit was run, which included markers interleukin-1a (IL-1a), interleukin-1beta  
512 (IL-1b), interleukin-17 alpha (IL-17a), and interleukin-33 (IL-33) (Cat. No. 740401, Biolegend). The standard instructions for the kit  
513 were used, with protein loaded at a fixed volume of 15 µL. After incubation, beads were run on the BD FACSVerser flow cytometer,  
514 and the data analysed using LEGENDplex™ Data Analysis software.

515 **Statistical analysis.** For histological staining, all data sets are n=3, with the exception of 2-week graphene, which is n=4, and 12  
516 weeks Neuronexus probes which are n=2, due to an inability to locate the probe location in histological sections for one animal  
517 implanted. For ELISA testing, gDNP with and without graphene hemisphere data sets are n=3 or 4 at all timepoints, while contralateral  
518 hemispheres were combined, giving n=7.

519

520

## References

- 522 1. Van Someren, E. J. W., Van Der Werf, Y. D., Roelfsema, P. R., Mansvelder, H. D. & Lopes da Silva, F. H. Slow brain oscillations of sleep, resting state, and  
523 vigilance. in *Progress in Brain Research* **193**, 3–15 (2011).
- 524 2. Lauritzen, M. *et al.* Clinical relevance of cortical spreading depression in neurological disorders: Migraine, malignant stroke, subarachnoid and intracranial  
525 hemorrhage, and traumatic brain injury. *Journal of Cerebral Blood Flow and Metabolism* **31**, 17–35 (2011).
- 526 3. Hughes, S. W., Lorincz, M. L., Parri, H. R. & Crunelli, V. Infraslow (<0.1Hz) oscillations in thalamic relay nuclei. basic mechanisms and significance to health

- 527 and disease states. in *Progress in Brain Research* **193**, 145–162 (2011).
- 528 4. Jirsa, V. K., Stacey, W. C., Quilichini, P. P., Ivanov, A. I. & Bernard, C. On the nature of seizure dynamics. *Brain* **137**, 2210–2230 (2014).
- 529 5. Nelson, M. J., Pouget, P., Nilsen, E. A., Patten, C. D. & Schall, J. D. Review of signal distortion through metal microelectrode recording circuits and filters. *J. Neurosci. Methods* **169**, 141–157 (2008).
- 530
- 531 6. Masvidal-Codina, E. *et al.* High-resolution mapping of infraslow cortical brain activity enabled by graphene microtransistors. *Nat. Mater.* **18**, 280–288
- 532 (2019).
- 533 7. Kostarelos, K., Vincent, M., Hebert, C. & Garrido, J. a. Graphene in the Design and Engineering of Next-Generation Neural Interfaces. *Adv. Mater.* **29**, 1–7
- 534 (2017).
- 535 8. Blaschke, B. M. *et al.* Mapping brain activity with flexible graphene micro-transistors. *2D Mater.* **4**, (2017).
- 536 9. Hébert, C. *et al.* Flexible Graphene Solution-Gated Field-Effect Transistors: Efficient Transducers for Micro-Electrocorticography. *Adv. Funct. Mater.*
- 537 **1703976**, 1703976 (2017).
- 538 10. Weltman, A., Yoo, J. & Meng, E. Flexible, penetrating brain probes enabled by advances in polymer microfabrication. *Micromachines* **7**, (2016).
- 539 11. Tien, L. W. *et al.* Silk as a multifunctional biomaterial substrate for reduced glial scarring around brain-penetrating electrodes. *Adv. Funct. Mater.* **23**,
- 540 3185–3193 (2013).
- 541 12. Zijlmans, M. *et al.* High-frequency oscillations as a new biomarker in epilepsy. *Ann. Neurol.* **71**, 169–78 (2012).
- 542 13. Jacobs, J. *et al.* High-frequency oscillations (HFOs) in clinical epilepsy. *Progress in Neurobiology* **98**, 302–315 (2012).
- 543 14. Staba, R. J., Stead, M. & Worrell, G. A. Electrophysiological Biomarkers of Epilepsy. *Neurotherapeutics* **11**, 334–346 (2014).
- 544 15. Wu, S. *et al.* Role of ictal baseline shifts and ictal high-frequency oscillations in stereo-electroencephalography analysis of mesial temporal lobe seizures.
- 545 *Epilepsia* **55**, 690–698 (2014).
- 546 16. Ikeda, A. *et al.* Focal ictal direct current shifts in human epilepsy as studied by subdural and scalp recording. *Brain* **122**, 827–838 (1999).
- 547 17. Bahari, F. *et al.* Spreading Depression and Seizure Unification Experimentally Observed in Epilepsy. *bioRxiv* **2**, (2018).
- 548 18. Duan, X. *et al.* Intracellular recordings of action potentials by an extracellular nanoscale field-effect transistor. *Nat. Nanotechnol.* **7**, 174–179 (2012).
- 549 19. Hess, L. H. Graphene Transistors for Biosensing and Bioelectronics. *Proc. IEEE* **101**, 1780–1792 (2013).
- 550 20. Hess, L. H. *et al.* High-transconductance graphene solution-gated field effect transistors. *Appl. Phys. Lett.* **99**, (2011).
- 551 21. Garcia-Cortadella, R. *et al.* Distortion-Free Sensing of Neural Activity Using Graphene Transistors. *Small* **16**, (2020).
- 552 22. Jin, H. J. *et al.* Water-stable silk films with reduced  $\beta$ -sheet content. *Adv. Funct. Mater.* **15**, 1241–1247 (2005).
- 553 23. Rockwood, D. N. *et al.* Materials fabrication from Bombyx mori silk fibroin. *Nat. Protoc.* **6**, 1612–31 (2011).
- 554 24. Vepari, C. & Kaplan, D. L. Silk as a biomaterial. *Prog. Polym. Sci.* **32**, 991–1007 (2007).
- 555 25. Cao, Y. & Wang, B. Biodegradation of silk biomaterials. *Int. J. Mol. Sci.* **10**, 1514–1524 (2009).
- 556 26. Gobin, A. S., Froude, V. E. & Mathur, A. B. Structural and mechanical characteristics of silk fibroin and chitosan blend scaffolds for tissue regeneration. *J. Biomed. Mater. Res. - Part A* **74**, 465–473 (2005).
- 557
- 558 27. Lecomte, A. *et al.* Silk and PEG as means to stiffen a parylene probe for insertion in the brain: Toward a double time-scale tool for local drug delivery. *J. Micromechanics Microengineering* **25**, (2015).
- 559
- 560 28. Fueta, Y. & Avoli, M. Effects of antiepileptic drugs on 4-aminopyridine-induced epileptiform activity in young and adult rat hippocampus. *Epilepsy Res.* **12**,
- 561 207–215 (1992).
- 562 29. Padmanabhan, K. & Urban, N. N. Disrupting information coding via block of 4-AP-sensitive potassium channels. *J. Neurophysiol.* **112**, 1054–1066 (2014).
- 563 30. Zakharov, A., Chernova, K., Burkhanova, G., Holmes, G. L. & Khazipov, R. Segregation of seizures and spreading depolarization across cortical layers.
- 564 *Epilepsia* **60**, 2386–2397 (2019).
- 565 31. Hartings, J. A. *et al.* Direct current electrocorticography for clinical neuromonitoring of spreading depolarizations. *J. Cereb. Blood Flow Metab.* **37**, 1857–
- 566 1870 (2017).
- 567 32. Harriott, A. M., Takizawa, T., Chung, D. Y. & Chen, S. P. Spreading depression as a preclinical model of migraine. *Journal of Headache and Pain* **20**, (2019).
- 568 33. Buzsáki, G. & Silva, F. L. da. High frequency oscillations in the intact brain. *Progress in Neurobiology* **98**, 241–249 (2012).
- 569 34. Chaudhary, U. J. *et al.* Mapping preictal and ictal haemodynamic networks using video- electroencephalography and functional imaging. *Brain* **135**, 3645–
- 570 3663 (2012).
- 571 35. Kamarajan, C., Pandey, A. K., Chorlian, D. B. & Porjesz, B. The use of current source density as electrophysiological correlates in neuropsychiatric

- 572 disorders: A review of human studies. *Int. J. Psychophysiol.* **97**, 310–322 (2015).
- 573 36. Coenen, A. M. L. & Van Luijckelaer, E. L. J. M. Genetic Animal Models for Absence Epilepsy: A Review of the WAG/Rij Strain of Rats. *Behavior Genetics* **33**,  
574 635–655 (2003).
- 575 37. Coenen, A. M. L. & Van Luijckelaer, E. L. J. M. The WAG/Rij rat model for absence epilepsy: age and sex factors. *Epilepsy Res.* **1**, 297–301 (1987).
- 576 38. Terlau, J. *et al.* Spike-wave discharges in absence epilepsy: segregation of electrographic components reveals distinct pathways of seizure activity. *J.*  
577 *Physiol.* (2020). doi:10.1113/JP279483
- 578 39. Dreier, J. P. *et al.* Spreading convulsions, spreading depolarization and epileptogenesis in human cerebral cortex. *Brain* **135**, 259–275 (2012).
- 579 40. Vanhatalo, S. *et al.* Very slow eeg responses lateralize temporal lobe seizures: An evaluation of non-invasive DC-EEG. *Neurology* **60**, 1098–1104 (2003).
- 580 41. Aiba, I. & Noebels, J. L. Spreading depolarization in the brainstem mediates sudden cardiorespiratory arrest in mouse SUDEP models. *Sci. Transl. Med.* **7**,  
581 (2015).
- 582 42. Loonen, I. C. M. *et al.* Brainstem spreading depolarization and cortical dynamics during fatal seizures in Cacna1a S218L mice. *Brain* **142**, 412–425 (2019).
- 583 43. Zhang, B. *et al.* Low-temperature chemical vapor deposition growth of graphene from toluene on electropolished copper foils. *ACS Nano* **6**, 2471–2476  
584 (2012).
- 585 44. Russo, E. *et al.* Upholding WAG/Rij rats as a model of absence epileptogenesis: Hidden mechanisms and a new theory on seizure development.  
586 *Neuroscience and Biobehavioral Reviews* **71**, 388–408 (2016).

587

## 588 Acknowledgments

589 **Funding:** This work has been funded by the European Union’s Horizon 2020 research and innovation programme under Grant  
590 Agreement No 785219 (Graphene Flagship). The ICN2 is supported by the Severo Ochoa Centres of Excellence programme, funded  
591 by the Spanish Research Agency (AEI, grant no. SEV-2017-0706), and by the CERCA Programme / Generalitat de Catalunya. A.B.C.  
592 is supported by the International PhD Programme La Caixa - Severo Ochoa (Programa Internacional de Becas "la Caixa"-Severo  
593 Ochoa). This work has made use of the Spanish ICTS Network MICRONANOFABS partially supported by MICINN and the ICTS  
594 ‘NANBIOSIS’, more specifically by the Micro-NanoTechnology Unit of the CIBER in Bioengineering, Biomaterials and  
595 Nanomedicine (CIBER-BBN) at the IMB-CNM. This work is within the project FIS2017-85787-R funded by the “Ministerio de  
596 Ciencia, Innovación y Universidades” of Spain, the “Agencia Estatal de Investigación (AEI)” and the “Fondo Europeo de Desarrollo  
597 Regional (FEDER/UE)”. A.B.C. acknowledges that this work has been done in the framework of the PhD in Electrical and  
598 Telecommunication Engineering at the Universitat Autònoma de Barcelona.

599 R.W. is funded by a Senior Research Fellowship awarded by the Worshipful Company of Pewterers

600 D. R. is a Biotechnology and Biological Sciences Research Council (BBSRC) LIDo sponsored PhD student.

601 The authors would like to thank Prof. Matthew Walker and Prof. Louis Lemieux (UCL Queen Square Institute of Neurology) for their  
602 comments on the manuscript.

603

604 **Author contributions:** A.B.C. carried out most of the fabrication and characterization of the gDNPs, contributed to the design and  
605 performance of the in vivo experiments, analysed the data and wrote the manuscript. E.M.C. contributed to the design and planning  
606 of the in vivo experiments and support to the SD analysis of the in vivo data. R.W., T.M.S. performed the in vivo experiments. D.R.,  
607 contributed to the in vivo experiments and DC-coupled recordings with the glass micropipette. N.S., E.R.L., X.I. and J.M.D.C.  
608 contributed to the fabrication and characterization of the gDNPs. E.D.C., J.B. and C.H., contributed to the growth, transfer and  
609 characterisation of CVD graphene used in the gDNPs. E.P.A., A.H. and E.R.L., contributed to the optimisation of the silk-fibroin  
610 stiffening protocol of the gDNPs. J.M.A., contributed to the fabrication of the custom electronic instrumentation and development of  
611 a Python-based user interface. D.V. contributed to the python scripts and technical discussions. J.R.S. reviewed the manuscript. J.F.  
612 and J.S. contributed to the mechanical assessment of the silk-fibroin and the silk-fibroin back-coated gDNPs. M.D. performed all  
613 surgeries for the biocompatibility study. A.D. and K.B. contributed to the capture of histological images and image-processing and  
614 analysis. S.S. and K.B. contributed to the preparation and review of the manuscript. A.G.B. contributed in the design and fabrication  
615 of the custom electronic instrumentation, development of a custom gSGFET Python library and analysis of the data. R.V., K.K.,  
616 R.W., A.G.B., and J.A.G. participated in the design of the in vivo experiments and thoroughly reviewed the manuscript. All authors  
617 read and reviewed the manuscript.

618 **Competing interests:** C.G. is the owner of g.tec medical engineering GmbH and Guger Technologies OG.

619 **Data and materials availability:** Raw data from gDNP characterization, electrophysiological recordings as well as biocompatibility  
620 assessment will be shared upon request to the corresponding authors.

